# Conformational dynamics underlying slow inactivation in voltage-gated sodium channels

Katsumasa Irie[1*#], Shuo Han[2*], Sarah Applewhite[2], Yuki K. Maeda[1], Joshua Vance[2] and Shizhen Wang[2#]

[1] Department of Biophysical Chemistry, School of Pharmaceutical Science, Wakayama Medical University, Wakayama, 640-8156, Japan

[2] Division of Biological and Biomedical Systems, School of Science and Engineering, University of Missouri-Kansas City, Kansas City, MO 64110 USA

*Authors contributed to this work equally

[#]Corresponding to Katsumasa Irie (kirie@wakayama-med.ac.jp) and Shizhen Wang (wangshizhen@umkc.edu)

**Abstract**

Voltage-gated sodium (Nav) channels initiate and propagate action potentials in many excitable cells. Upon repetitive activation, the fraction of Nav channels available for excitation gradually decreases on a timescale ranging from seconds to minutes, a phenomenon known as slow inactivation. This process is crucial for regulating cellular excitability and firing patterns. Slow inactivation is proposed to result from the collapse of the selectivity filter pore coupled with the opening of the primary helix bundle crossing gate. However, the conformational changes underlying slow inactivation and the molecular coupling between the selectivity filter and primary gate remain unclear. In this study, we investigated the conformational dynamics of the selectivity filter in prokaryotic NavAb channels reconstituted into liposomes using single-molecule FRET (smFRET). Our smFRET data revealed the conformational transitions in the NavAb selectivity filter pore among three distinct states, with activating voltages enriching the high-FRET conformations, potentially associated with slow inactivation. Using electrophysiological and crystallographic methods, we further identified the L176 residue in the selectivity filter P1 helix as a critical coupler between the primary and slow inactivation gates. We showed that L176 mutations with side chains of larger sizes significantly facilitated the slow inactivation of the NavAb channel, and the L176F mutation forced the opening mutant carrying the C-terminal deletion to be crystallized at the closed state. Consistently, our smFRET results revealed that C-terminal deletion markedly attenuated the high FRET conformation of the selectivity filter, which was restored by the L176F mutation. Moreover, using the classical Nav open-pore blocker lidocaine, we showed that it also depleted the high FRET conformation of the NavAb selectivity filter in a dose-dependent manner. The L176F mutation, again, markedly reversed the conformational shifts caused by lidocaine, an effect similar to it on the opening mutant carrying the C-terminal deletion. Our studies consistently suggested that slow inactivation in the NavAb channel is underlined by the collapse of the selectivity filter pore, represented by the high FRET conformation uncovered by our smFRET measurements, while the L176 residue at the P1 helix of the selectivity filter and T206 at the pore lining helix couple the conformational changes of the slow inactivation gate at selectivity filter and the primary gate at the helix bundle crossing.

## Introduction

Voltage-gated sodium channels (Navs) mediate $Na^+$ diffusion across cell membranes to initiate action potentials essential for nerve firings or contractions of skeletal or cardiac muscle [1,2]. Dysfunction in Nav causes numerous channelopathies, including epilepsy, chronic pain syndromes and cardiac arrhythmias [3,4]. Immediately after activation, Navs quickly enter the fast inactivation state so the cell membrane potential can be repolarized to initiate another action potential [5]. The fast inactivation results from voltage-dependent blocking of $Na^+$ permeation pores by the linker carrying the 'IFM' motif, known as the fast inactivation gate, between domains III and IV of Nav channels [5,6]. Nav channels also undergo a distinct slow inactivation, which occurs over seconds to minutes, serving as a critical mechanism to prevent persistent nerve firings or muscle contractions [7].

Prokaryotic Nav channels are highly conserved in structure and function with eukaryotic orthologs [8,9]. Due to their simpler structures and amenability to crystallographic and cryo-EM analyses, studies on them have provided invaluable mechanistic insights into the ion selectivity, voltage gating and inactivation of Nav channels [10-13]. Prokaryotic Nav channels lack fast inactivation gates and, therefore, do not exhibit the fast inactivation typically seen in eukaryotic Nav channels, but their conductance to sodium, upon repetitive activation, does gradually decrease in the time scale of seconds to minutes, similar to the slow inactivation in eukaryotic Nav channels [9,14,15]. Indeed, electrophysiological analyses indicated that the collapse of the selectivity filter pore perhaps serves as a shared structural mechanism for slow inactivation in both prokaryotic and eukaryotic Nav channels [12,15-17]. However, the underlying mechanisms remain elusive, particularly lacking direct measurements of the conformational changes at the selectivity filter when Nav channels transit from activation to the inactivation state.

In the present work, we leverage NavAb as a structural model to uncover the real-time conformational dynamics of the selectivity filter and the effects of activating voltages to understand the molecular mechanisms driving slow inactivation. By implementing

smFRET measurements on NavAb channels reconstituted into liposomes, we showed that the selectivity filter pore transits among 3 distinct conformation states spontaneously, with activating voltages enriching the high FRET conformation. Moreover, we found that both C-terminal deletion and the blocker lidocaine, which stabilize NavAb channels at the opening state, diminished the high FRET conformations, matching their functional roles well in attenuating slow inactivations. In addition, we identified Leu176 as the critical residue coupling the primary and slow inactivation gates. We showed that the L176F mutation stabilized the open C-terminal deletion mutant at the closed state in the crystal structure and also promoted the high FRET conformation in the selectivity filter. Our smFRET studies, combined with electrophysiological and crystallographic analyses, consistently indicated that the high FRET, constricted conformation in the selectivity filter represents the slow inactivated state, with L176 and T206 mediating conformational talk between the primary gate at bundle crossing and the slow inactivation gate at the selectivity filter.

## Results

*1. Activating voltages alter the conformational landscapes of the NavAb selectivity filter.*

The conformational changes associated with slow inactivation in the NavAb channel remain unclear, perhaps too dynamic to be determined by crystallographic or cryoEM studies. Thus, we implemented smFRET on NavAb channels reconstituted into liposomes to uncover the structural dynamics underlying slow inactivation. To achieve the studies, we constructed and purified functional tandem dimeric NavAb channel proteins [18], which carry cysteine mutations at either E189 or V190 residues at the P2 helix, so that the two cysteines in a tetrameric channel are located at the diagonal subunits (Fig. 1a). The Cy3 and Cy5 FRET fluorophore pair carrying maleimide reactive groups were conjugated to the two cysteine residues, their FRET changes will report the real-time conformational changes of the NavAb selectivity filter. By reconstituting NavAb proteins into liposomes, we were able to apply three different electrical potentials on NavAb channel proteins, i.e.,-85, 0, and 120 mV, generated by intra- and extraliposomal $K^+$ gradients of 5/150, 5/5 and 5/0.04 mM, in the presence of valinomycin (Fig. 1b). This method has been successfully used in our previous studies on voltage-gated proton channels [19,20]. The wild-type NavAb is inactivated even at deep potentials, but the N49K mutation shifts the activation curve by 75 mV to a half-activation voltage of -22 mV [10,14]. Therefore, in this study, the N49K background mutation (named BG in all figures if no other mutations were introduced) was introduced into all mutants so they are at deactivated, partially activated or fully activated states under -85, 0 or 120 mV, respectively. Importantly, tandem dimeric NavAb constructs carrying the V190C mutation expressed in SF-9 cells produced functional channels (Extended Fig. 1a and b), and purified tandem dimeric NavAb proteins were also functional, as reported in our previous study [18]. Our smFRET measurements clearly showed that FRET between Cy3/Cy5 fluorophores labeling at V190C residues at the diagonal subunits exhibit spontaneous transitions among 3 distinct states, suggesting that the NavAb selectivity filter pores may undergo remarkable conformational changes (Fig 1c, extended Fig 2a). Importantly, similar changes were also observed by switching the fluorophore labeling sites to the adjacent E189C (Fig. 1c and extended Fig. 2a). The

smFRET data from either the E189C or V190C labeling sites under voltages -85, 0, and 120 mV all demonstrated 3 major FRET peaks with centers at 0.25, 0.55, and 0.8, named as low, medium, and high FRET populations, respectively (Fig. 1d and e). From both labeling sites, the high FRET populations with peak center ~0.8 were significantly enriched by strong activating voltages (Fig. 1d, e and f). It is also worth noting that the peak centers of both the low and high FRET populations from the E189C site are slightly higher than those from the V190C site, matching well with the fact that the distance between the two diagonal E189C residues is closer than the two diagonal V190C residues (Fig. 1a). Since strong activating voltages enrich the high FRET population, it is reasonable to assume that it may represent the NavAb selectivity filter conformation at the inactivated state.

To further determine the functional association of FRET changes at the NavAb selectivity filter, we introduced the T206A background mutation, which was shown to attenuate the late, use-dependent slow inactivation of the NavAb channel [16]. Our smFRET data indeed showed that the T206A mutation depletes the high FRET population significantly under -85 mV, matching with its functional effects to attenuate slow inactivation in NavAb channels (extended Fig. 2b and c). However, significant enrichments of the high FRET population were also observed from the E189C labeling sites carrying the T206A mutation under strong activating voltages. All the smFRET data above consistently suggested that high FRET conformational populations represent the NavAb selectivity filter conformations at the inactivated state.

2. *Mutations at the selectivity filter and C-terminus change the slow inactivation in the NavAb channels.*

L176 is located at the bottom of the NavAb selectivity filter, in close proximity to the S6 helix, which forms the inner cavity of the channel pore. We hypothesized that bending and rotation of the S6 helix, a conformational transition essential for opening the primary gate at the helix bundle crossing, may alter the selectivity filter conformation through L176. Indeed, our electrophysiological data indicated that mutations to bulky side chain residues

like Phe (L176F) and Trp (L176W) significantly altered the slow inactivation of NavAb channels (Fig. 2a and extended Fig. 3a, b, c). The voltage dependencies of L176F and L176W activation were almost unchanged, while their half-inactivation voltages were shifted negatively by over 30 mV (extended Fig. 3a, b, c, and Table 1). The S6 helix is a long and uninterrupted α-helix impacting both activation and slow inactivation of the NavAb channel [21]. The cytosolic helix bundle formed by four S6 helices of a tetrameric NavAb channel is a structural feature shared among prokaryotic Navs [22]. Deletion of the S6 helix bundle enhances the early phase of the slow inactivation, meanwhile blocking the late use-dependent inactivation of the NavAb channel [16,22]. We also observed similar changes in slow inactivation from the mutant used in the present work, which carries a C-terminal deletion to Q230, named ΔC230 (Fig. 1a, Fig. 2a, extended Fig. 3d) [16].

We obtained crystal structures of the NavAb channel carrying the N49K background mutation (named BG hereafter) and those containing additional mutations, including L176F, ΔC230, ΔC230/L176F and L176W (Fig. 2b). The L176F and L176W mutations increased the overall temperature factor and decreased the resolution of full-length structures, but L176F mutant demonstrated opposite effects on the ΔC230 mutants, implying the potential interactions between the primary gate and selectivity filter (Extended Table 1). The overall RMSD of all structures before the S6 helix is below 1Å, indicating there is very minimal overall structural change in all mutants (Fig. 2c, d). Moreover, despite their differences in inactivation behaviors, no changes were observed in the selectivity filter for all these mutants (Fig. 2b, d)

Around the S6 helix, the RMSD of ΔC230 was greater than 1Å, indicating that the primary gate was closed in the full-length but opened in the ΔC230 structures (Fig. 3a, b). The primary gate in the ΔC230/L176F crystal structure, surprisingly, was closed like those of full-length channels (Fig. 3a, b). In all crystal structures, it is clear that residues at the 176 position were very close to T206 in the S6 helix (Fig. 2b). In the ΔC230 structure, T206 moved towards L176 by more than 1Å (Fig. 3c). However, T206 residues of the structures of L176F and ΔC230/L176F mutants are superimposed very well with that of BG structure (Fig. 3d), and their proximity to L176 also have no difference, as indicated

by the distances from the T206 Cβ carbon to the L176 Cγ, Cβ, and Cα carbons (Table 2). These structures indicated that the L176F side chain forced the primary gate of the ΔC230 mutant to close through steric hindrance with the T206 in the S6 helix. Consistently, in the structure of the L176W mutant, the more bulky Trp side chain pushed the T206 further away by ~1Å, in comparison to the structure of L176F (Fig. 3e and Table 2). The bulkier Trp residue, perhaps, has also prevented us from obtaining crystals of the ΔC230/L176W mutant.

In summary, the primary and slow inactivation gates in all these structures were likely decoupled, or the primary gate was not opened sufficiently, which could not render the selectivity filter an inactivated state.

*3. A critical residue in the P1 helix mediates crosstalk between the selectivity filter and primary gates*

From the crystallographic analyses above, even though we were not able to uncover the slow inactivated selectivity filter conformation, the finding that the L176F mutation closes the primary gate of the ΔC230 mutant clearly demonstrates the strong conformational couplings between the primary helix bundle crossing gate and the selectivity filter inactivation gate. Expression of tandem dimeric NavAb constructs carrying the L176F mutation or ΔC230 deletion produced functional channels in SF-9 cells (Extended Fig. 1d, e). Therefore, we further examined the effects of the L176F and C-terminal deletion on the conformational dynamics of the selectivity filter by smFRET. Consistent with crystal structures, no obvious changes in the FRET distributions at either V190C or E189C labeling sites were induced by L176F mutation, yet strong activating voltages still significantly enriched their high FRET populations (extended Fig. 2d-g). Since smFRET data from the E189C and V190C labeling sites matched well, we only used the V190C labeling site in the following studies. Dramatic changes, however, were observed from the ΔC230 mutant, where the high FRET population was almost absent, and enrichment effects of strong activating voltages were also very minimal, which are completely different from smFRET results collected on the BG, L176F, or T206A mutants

(Fig. 4a, b). It was reported that the C-terminal deletion blocks late, use-dependent slow inactivation [16]. Our results from the ΔC230 mutant suggested that the high FRET conformation may be associated with the late use-dependent inactivated state rather than the early phase of the slow inactivation. Intriguingly, we found that introducing the L176F mutation into the ΔC230 mutant markedly enhanced the medium FRET population but not the high FRET population (Fig. 4c, d). Since both T206 and L176 mutations primarily impact the early phase of slow inactivation, the medium FRET populations may represent the early phase of slow inactivation. The fact that the L176F mutation promotes the medium FRET conformation in the ΔC230 mutant provides another piece of evidence in support of its critical role in mediating conformational changes between the slow inactivation and primary gates by interacting with T206.

*4. Open-channel blocker lidocaine alters the NavAb selectivity filter dynamics in the same way as open mutation.*

As a classical open-channel blocker of eukaryotic Nav channels, lidocaine was found to prevent Nav1.5 and Nav1.7 channels from entering into the slow inactivation state [23,24]. Lidocaine was also shown to block prokaryotic NavAb channels with high affinities at the inner cavity immediately underneath the selectivity filter pore [25]. In the present work, we also examined the effects of lidocaine on the selectivity filter conformation using smFRET. Our results showed that the high FRET conformations were almost markedly depleted by 5 mM lidocaine (Fig. 4e), a change very similar to those caused by the deletion of the C-terminal helix bundle. More importantly, the conformational effects of lidocaine exhibit a clear concentration-dependent manner, with a half-effective concentration close to 0.1 mM, similar to that determined by electrophysiological studies [25] (Fig. 4e, f). The observed effects of lidocaine on NavAb selectivity filter conformation matched well with its functional results of preventing Nav channels from entering the slow inactivation state, supporting that high FRET conformation represents the selectivity filter at the inactivated state. Interestingly, a high FRET population was also present in the NavAb channel carrying the L176F mutation, even with 5 mM lidocaine. (Fig. 4e, f). Our smFRET data collectively suggested that high-FRET conformation underlies the late, use-dependent, slow

inactivation of the NavAb channel, while the medium FRET may underlie the early phase of slow inactivation.

## Discussions

Slow inactivation is a key mechanism of Navs for regulating the frequencies of nerve firings and muscle contractions [7]. Residues at the selectivity filter, pore, and voltage sensor domains in Navs were found to impact slow inactivation, but the underlying structural basis remains elusive. Many studies suggested slow inactivation as the collapse of the selectivity filter pore, a mechanism quite similar to C-type inactivation in potassium channels [26,27]. However, the conductive state of the potassium channel selectivity filter pore can be inferred from its ion occupancy profiles, but the functional status of Nav selectivity filters has yet to be determined.

In the prokaryotic NavAb channel, electrophysiological studies showed that there are multiple phases of slow inactivation [9,16], but their underlying structural mechanisms remain unclear. In the present work, we conjugated Cy3/Cy5 FRET at diagonal E189C or V190C residues at the P2 helix in the selectivity filter. Therefore, the Cy3/Cy5 FRET reports the relative movements of the P2 helix, presumably the selectivity filter. Our smFRET data from both the E189C and V190C labeling sites consistently indicated that there are a minimum of 3 distinct FRET states, named low, medium, and high FRET populations. First of all, the conformational dynamics of the NavAb selectivity filter are very different from those of a potassium channel, which are very rigid, suggesting a fundamental difference in their structural basis underlying ion selectivity [28]. Our smFRET data collected from the NavAb channel, from multiple labeling sites, clearly showed that high FRET populations of its selectivity filter were (a) enriched by strong activating voltages, (b) attenuated by the S6 helix mutation T206A attenuating the slow inactivation, (c) restored by the selectivity filter mutation L176F promoting slow inactivation, (d) diminished by the C-terminal deletion, (e) diminished by the lidocaine, which was found to prevent Nav channels from entering slow inactivation state. All these data consistently support the idea that the high FRET constricted selectivity filter conformations may be

associated with late use-dependent slow inactivation in the NavAb channel, while low FRET conformations may represent the dilated selectivity filter pore conformation, which is conductive (Fig. 5). The medium FRET conformation, however, could be a unique conformational state associated with early phases of slow inactivation in the NavAb channel. Considering that lidocaine acts as an open-state blocker, the medium FRET conformation could also correspond to the open conformation or an intermediate one between the open state and the early phase of slow inactivation. The FRET Cy3/Cy5 fluorophore pair actually reports the relative movements between two diagonal P2 helices. Therefore, another possible interpretation is that the medium FRET conformation could represent an asymmetric selectivity filter pore, with one subunit adopting the high FRET inactivated conformation and one adopting the low FRET conductive conformation. Then, the late use-dependent slow inactivation could be a deep inactivated state with 2 or more selectivity filters in a tetrameric channel unit, adopting the high FRET inactivated conformation. The selectivity filters of the eukaryotic Nav channels are asymmetrical [29]. It would be interesting to examine the conformational dynamics of the selectivity filter from each homolog domain and their roles in the early and late phases of the slow inactivation.

There are multiple NavAb crystal structures proposed to be in potentially inactivated states exhibiting unusual 2-fold symmetry, but their primary gate apparently does not open sufficiently to conduct ions [13]. Similarly, the selectivity filter of the opened NavAb structure does not differ significantly from that of the locked at the closed state [11,21]. From all the available NavAb structures, no coupled conformational changes were identified between the primary and the inactivated gates, which is the hallmark feature of slow inactivation [7,17]. It is possible that the primary gates of all ‘opening’ NavAb structures were not open sufficiently to render the selectivity filter a slow inactivated conformation. In the KcsA potassium channel, its selectivity filter does not transit to the inactivated conformation until the primary helix bundle crossing gate opens over 20 angstroms [26,27]. In this sense, we may have a better chance to capture the inactivated NavAb selectivity filter from mutants carrying a reinforced coupler like the L176F if conditions can be found to open its primary gate sufficiently wide. Recent cryo-EM analyses on a homotetrameric NavEh channel, cloned from eukaryotic single-cell algae, revealed remarkable changes

at the P2 helix in the selectivity filter between potential slow inactivated and non-inactivated state channels [12]. These structures suggested that the inactivated selectivity filter of the NavEh channel adopted a more dilated conformation. Oddly, the primary gate of the NavEh channel in the presumptive inactivated state was not open, while that of the presumptive non-inactivated channel was not closed. Suppose the NavEh WT channel with the constricted selectivity filter pore and open primary gate actually represents the channel in the inactivated state. In that case, it is consistent with our smFRET results, i.e., the high FRET constricted conformation represents the inactivated selectivity filter.

## Materials and Methods

### *Site-directed mutagenesis and construction of NavAb mutants*

The NavAb mutated DNAs were subcloned into the modified pBiEX-1 vector (Novagen) that was modified by replacing the fragment from the NdeI site to the SalI site in the multi-cloning site with that of the previously described modified pET-15b (Novagen) vector between BamHI and SalI [30,31]. The polymerase chain reaction accomplished site-directed mutagenesis using PrimeSTAR® Max DNA Polymerase (Takara Bio). All clones were confirmed by DNA sequencing. The plasmids expressing tandem dimeric NavAb proteins were constructed by inserting 2 copies of NavAb cDNAs into the pET28a vector at NdeI-BamHI and BamHI-SalI sites, with a flexible linker sequence encoding double 'GGGS' and the FLAG tag [18].

### *Electrophysiological measurement in insect cells*

The recordings were performed using SF-9 cells. SF-9 cells (ATCC#CRL-1711) were grown in Sf-900™ II medium (Gibco) complemented with 1% 100× Antibiotic-Antimycotic (Fujifilm-Wako) at 27°C. Cells were transfected with target channel-cloned pBiEX vectors and enhanced green fluorescent protein (EGFP)-cloned pBiEX vectors using polyethyleneimine (PEI) reagent [30,31]. PEI was solubilized into distilled water, and the pH of the 1 mg/mL PEI solution was adjusted to 7.0 with NaOH. First, the channel-cloned vector (3.3 μg) was mixed with 1.6 μg of the EGFP-cloned vector in 150 μL of the

culture medium. Next, 15 μL 1mg/mL PEI solution was added, and the mixture was incubated for 10 min before the transfection mixture was gently dropped onto cultured cells. After 24-48 h incubation, the cells were used for electrophysiological measurements. Cancellation of the capacitance transients and leak subtraction were performed using a programmed P/10 protocol delivered at -140 mV. The bath solution was changed using the Dynaflow® Resolve system. All experiments were conducted at 25 ± 1°C using a whole cell patch clamp recording mode with a HEKA EPC 10 amplifier and Patch master data acquisition software (v2x73). Data export was done using Igor Pro 9.05 and NeuroMatic (version 3.0b). All sample numbers represent the number of individual cells used for each measurement. Cells with leak currents less than 1 nA were used for measurements. When any outliers were encountered, these outliers were excluded if any abnormalities were found in other measurement environments and were included if no abnormalities were found. All results are presented as mean ± SE. The graph data were plotted using SigmaPlot 14.

*Protein expression and purification*

Proteins were expressed in the Escherichia coli KRX strain (Promega). Cells were grown at 37ºC to an $OD_{600}$ of 0.6, induced with 0.1% rhamnose (Fujifilm-Wako), and grown for 16 h at 20ºC. The cells were suspended in TBS buffer (20 mM Tris-HCl pH 8.0, 150 mM NaCl) and lysed using LAB1000 (SMT Co., LTD.) at 12,000 psi. Low-speed centrifugation removed cell debris (12,000×g, 30 min, 4°C). Membranes were collected by centrifugation (100,000×g, 1 h, 4°C) and solubilized by homogenization in TBS buffer containing 30 mM n-dodecyl-β-D-maltoside (DDM, DOJINDO). After centrifugation (40,000×g, 30 min, 4°C), the supernatant was loaded onto a HIS-Select® Cobalt Affinity Gel column (Sigma). The protein bound to the cobalt affinity column was washed with 10 mM imidazole in TBS buffer containing 0.05% lauryl maltose neopentyl glycol (LMNG, Anatrace) instead of DDM. After washing, the protein was eluted with 300 mM imidazole, and the His tag of the protein samples for crystallization was removed by thrombin digestion (overnight, 4°C). Eluted protein was purified on a TSKgel G4000SWXL (TOSO Corp.) in TBS buffer containing 0.05% LMNG.

*Crystallization and structural determination*

Before crystallization, the purified protein was concentrated to ~10mg ml-1 and reconstituted into a bicelle solution containing a 10% bicelle mixture at 2.8:1 (1,2-dimyristoyl-sn-glycero-3-phosphorylcholine [DMPC, Anatrace]: 3-[(3-cholamidopropyl) dimethylammonio]-2-hydroxy propane sulfonate [CHAPSO, DOJINDO]). The 10mg/ml protein solution of NavAb and 10% bicelle were mixed in a 20:1 ratio. Prepared proteins of the full-length NavAb mutants were crystallized by sitting-drop vapor diffusion at 20°C by mixing 300-nl volumes of the protein solution (8–10 mg/ml) and the reservoir solution (9%–11% polyethylene glycol monomethyl ether [PEG MME] 2000, 100 mM sodium chloride, 100 mM magnesium nitrate, 25mM cadmium chloride and 100 mM Tris-HCl, pH 8.4) with mosquito LCP (STP Labtech). The crystals were grown for 1 to 3 weeks, and after growing, the crystals were transferred into the reservoir solution without cadmium nitrate, which was replaced with the following cryoprotectant solutions. The cryoprotectant solution contains 11% PEG MME 2000, 100 mM Tris-HCl pH 8.4, 2.5 M sodium chloride, 100 mM magnesium nitrate, 0.05% LMNG, and 20% (v/v) DMSO.

Prepared proteins of C-terminal deletion NavAb mutants were crystallized by sitting-drop vapor diffusion at 20°C by mixing 300-nl volumes of the protein solution (8–10 mg/ml) and the reservoir solution (7%–9% PEG 6000, 100 mM sodium chloride, 100 mM magnesium nitrate, 100mM cadmium chloride, 10mM copper chloride and 100 mM Tris-HCl, pH 8.4) with mosquito LCP (STP Labtech). The crystals were grown for 1 to 3 weeks, and after growing, the crystals were transferred into the reservoir solution without cadmium nitrate, which was replaced with the following cryoprotectant solutions. The cryoprotectant solution contains 11% PEG 6000, 100 mM Tris-HCl pH 8.4, 2.5 M sodium chloride, 100 mM magnesium nitrate, 0.05% LMNG, and 20% (v/v) DMSO.

All crystallography data were automatically collected at BL41XU and BL45XU of SPring-8 and merged using the ZOO system [32]. The data were processed by the KAMO system [33] with XDS (version 20220110) [34]. The data sets of the NavAb BG were obtained from a single crystal. The data sets of the L176F and L176W mutants of NavAb were

obtained from multiple crystals. Analyses of the data with the STARANISO server (Global Phasing Ltd) [35] revealed severely anisotropic crystals. Therefore, the data sets were ellipsoidally truncated and rescaled to minimize the inclusion of poor diffraction data.

A molecular replacement method with PHASER [36] provided the initial phase using the structure of NavAb N49K mutant (pdb code: 5yuc) as the initial model. The final model was constructed in COOT (version 0.9.2) [37] and refined in Phenix (version 1.18) [38]. CCP4 package (version 7.0.078) [39] was used for Structural analysis. Supplementary Table 1 summarizes data collection and refinement statistics for all crystals. All figures in the present paper were prepared using the program PyMOL 2.5.4 (Schrödinger, LLC, 2015:The PyMOL Molecular Graphics System, Version 1.8). The pore radii were calculated using the HOLE program [40].

*Fluorophore labeling, liposome reconstitution and smFRET imaging*

NavAb proteins carrying either E189C or V190C mutations were conjugated with photostable Cy3/Cy5 c5 maleimide (1:1) as described previously [18,41]. The fluorophore-labeled NavAb proteins were then reconstituted into liposomes containing POPE/POPG (3:1, w/w, Avanti Polar Lipids Inc.) with a protein lipid ratio of 1:4,000 (w/w) using Bio-beads SM2 (Bioad Inc.) to remove detergents, and the NavAb proteoliposomes were either immediately used or stored in a -80 °C freezer. Immediately before smFRET imaging, the NavAb proteoliposomes were extruded through a 200 nm polycarbonate membrane >30 times to obtain unilamellar, uniform-size liposomes, then immobilized on PEG/biotin-PEG (98:2, w/w) passivated coverslip surfaces for imaging through biotinylated anti-Histag or anti-FLAG antibodies (ThermoFisher, MA1-21315-BTIN, MA1-91878-BTIN) [42]. SmFRET imaging was performed with an objective-based TIRF microscope, and liposomal electrical voltages were generated by transliposomal $K^+$ gradients ($K^+_{in}/K^+_{out}$, mM, 5/150 for -85 mV, 5/5 for 0 mV and 5/0.04 for 120 mV) in the presence of 0.45 μM valinomycin [20]. SmFRET movies were collected by an exciting laser of 532 nm (~1.0 W/cm$^2$) with a time resolution of 100 ms. The PCD/PCA oxygen scavenger system and ~3 mM Trolox were included in the imaging buffer to improve the

photostability of the fluorophores [43]. Raw smFRET movies without any corrections were processed by the SPARTAN software with the point spread function (PSF) window size of 7 pixels, and smFRET traces were selected using the Autotrace function and further manually inspected following the criteria described previously [20,44]. After correction of the crosstalk and gamma effect, smFRET traces were idealized using the Maximum Point Likelihood algorithm built into the SPARTAN software with a 4 FRET state model, including the low, medium, high FRET states and one additional zero FRET state accounting for the blinking and bleaching FRET events [45].

## Data Availability

The structural data generated in this study have been deposited in the Protein Data Bank under accession codes 9VDQ[https://doi.org/10.2210/pdb9VDQ/pdb]: Crystal structure of voltage-gated sodium channel NavAb N49K mutant, 9VDR[https://doi.org/10.2210/pdb9VDR/pdb]: Crystal structure of voltage-gated sodium channel NavAb N49K/L176F mutant, 9VDS[https://doi.org/10.2210/pdb9VDS/pdb]: Crystal structure of voltage-gated sodium channel NavAb N49K/L176W mutant, 9VDT[https://doi.org/10.2210/pdb9VDT/pdb]: Crystal structure of voltage-gated sodium channel NavAb N49K ΔC230 mutant, 9VDU[https://doi.org/10.2210/pdb9VDU/pdb]: Crystal structure of voltage-gated sodium channel NavAb N49K/L176F ΔC230 mutant. The structure of the NavAb N49K mutant for the initial model of molecular replacement was available in the Protein Data Bank under accession code 5YUC. The electrophysiologic data that support this study are available from the corresponding author, K.I., upon reasonable request.

## Acknowledgments

This work was funded by NIH grant 1R01GM142816 (SW). The synchrotron radiation experiments were performed at BL41XU and BL45XU in SPring-8 with the approval of the Japan Synchrotron Radiation Research Institute (JASRI) (Proposal numbers 2013B1178, 2015B1042, 2016B2721, 2017B2735, and 2018B2710). We thank the beamline staff for their excellent facilities and support. This research was partially supported by Platform Project for Supporting

Drug Discovery and Life Science Research (Basis for Supporting Innovative Drug Discovery and Life Science Research [BINDS]) from AMED under Grant Numbers JP21am0101070, JP22ama121001 and JP23ama121001. This work was supported by Grants-in-Aid for Scientific Research (17K17795, 21K19332, 20K09193, and 24K02168), SEI Group CSR Foundation, Takeda Science Foundation, and the Institute for Fermentation (KI).

## Author Contributions

SW and KI conceived the studies. SW and SH designed and performed smFRET studies and analyzed smFRET data with the help of SA and JV. KI designed and performed electrophysiological and crystallographic studies and analyzed these data. YM collected and analyzed electrophysiological data. SW and KI prepared the manuscript with editing input from other authors.

1 **Table 1. Half-inactivation and activation voltages of NavAb mutants**

| | Inactivation | | | | Activation | | | |
|---|---|---|---|---|---|---|---|---|
| | $V_h$ (mV) | slope factor | $I_{max}$ | Sample N | $V_h$ (mV) | slope factor | $G_{max}$ | Sample N |
| BG(N49K) | -111 ± 2 | -11.8 ± 1.6 | 1.00 ± 0.03 | 4 | -45.3 ± 1.5 | 3.73 ± 1.10 | 0.90 ± 0.03 | 4 |
| L176F | -160 ± 3 | -11.6 ± 1.4 | 1.14 ± 0.10 | 4 | -30.9 ± 3.2 | 10.5 ± 2.8 | 1.08 ± 0.05 | 7 |
| L176W | -187 ± 31 | -22.1 ± 5.8 | 2.41 ± 1.90 | 4 | -33.7 ± 2.0 | 7.96 ± 1.70 | 0.82 ± 0.02 | 4 |
| ΔC230 | -99.7 ± 1.0 | -6.53 ± 0.93 | 0.99 ± 0.04 | 5 | -35.3 ± 0.9 | 4.35 ± 0.70 | 0.87 ± 0.02 | 3 |

2 Half-inactivation voltage ($V_h$) is the membrane potential of 50% steady-state inactivation;
3 Half-activation voltage ($V_h$) is the membrane potential of 50% tail-current activation. All
4 results are expressed as mean ± S.E.

5

1 **Table 2. Root mean square deviation (RMSD) and distance between the 176**
2 **residues and T206 of the NavAb channels**

| | RMSD with BG mutant (Å) | | Distance from T206 Cβ to Nearest atom of 176 residues (Å) | Cγ | Cβ | Cα |
|---|---|---|---|---|---|---|
| | 176 Residues | Thr206 | | | | |
| BG | - | - | 6.6 | 6.9 | 8.4 | 9.0 |
| L176F | 0.30 | 0.68 | 4.1 | 6.8 | 8.3 | 8.9 |
| L176W | 0.70 | 0.79 | 4.8 | 7.8 | 9.2 | 9.9 |
| ΔC230 | 0.23 | 2.31 | 6.2 | 6.2 | 7.6 | 8.1 |
| ΔC230/L176F | 0.15 | 0.50 | 4.3 | 6.8 | 8.3 | 8.7 |

3

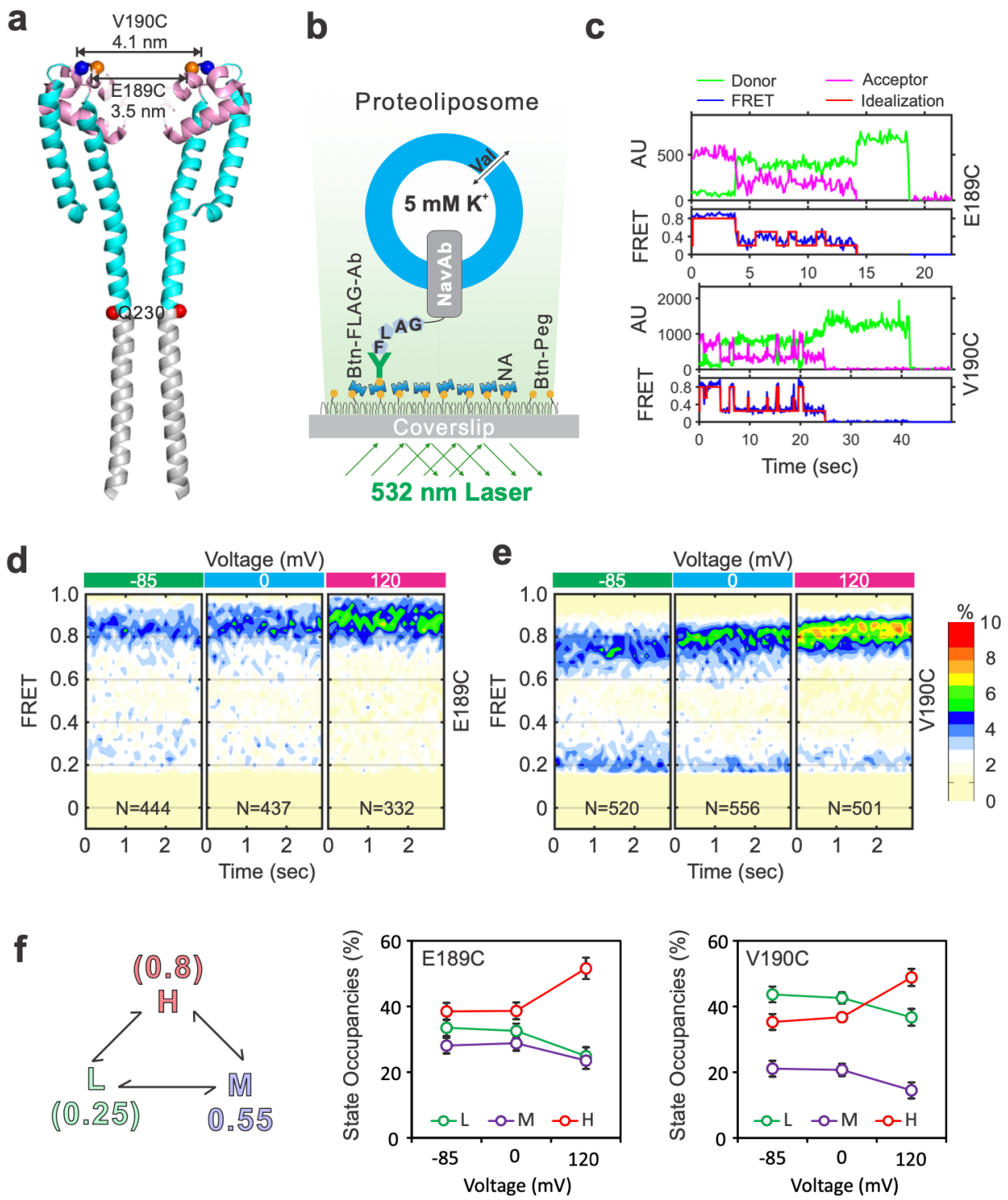


**Figure 1. Activating voltage induces the constricted conformation at the NavAb selectivity filter at the potential inactivation state**

**a**. Cartoon of the NavAb pore domain, with 2 subunits removed for clarity (PDB: 5VB2). The pore-forming helices are colored cyan, and the P1/P2 helices of the selectivity filter are colored pink. The C-terminal helices are colored gray. The Cα carbon atoms of E189C and V190C at diagonal subunits for fluorophore labeling were highlighted by orange and blue spheres, respectively. **b**. The experimental setup to examine conformational dynamics of the NavAb selectivity filter using smFRET. The fluorophore-labeled NavAb channels were reconstituted into liposomes (POPE/POPG=31, w/w), and the proteoliposomes were immobilized on the PEGylated surface through neutravidin and biotinylated anti-histag or anti-FLAG tag antibodies, so only those with the C-terminus of the NavAb channel facing outside were retained for smFRET imaging. Transliposomal electrical potentials were generated by transliposomal $K^+$ gradients and valinomycin, with the intraliposomal $K^+$ concentration as 5 mM and extraliposomal $K^+$ concentration as 150, 5, and 0.04 mM for -85, 0, and 120 mV, respectively. **c**. smFRET traces showed that FRET between Cy3/Cy5 fluorophores conjugated at E189C or V190C at the P2 helix in the NavAb selectivity filter exhibits transitions among 3 distinctive states. **d-e**. Contour maps of smFRET traces collected from E189C (**d**) and V190C (**e**) labeling sites indicated that strong activating voltages enriched the high FRET populations. **f**. The kinetic model for analyzing smFRET traces collected from E189C and V190C labeling sites. smFRET traces were idealized into low, medium and high FRET states with peak centers at 0.25, 0.55 and 0.8. The FRET state occupancy data clearly showed that strong activating voltages enriched the high FRET state but diminished the medium and low FRET states.

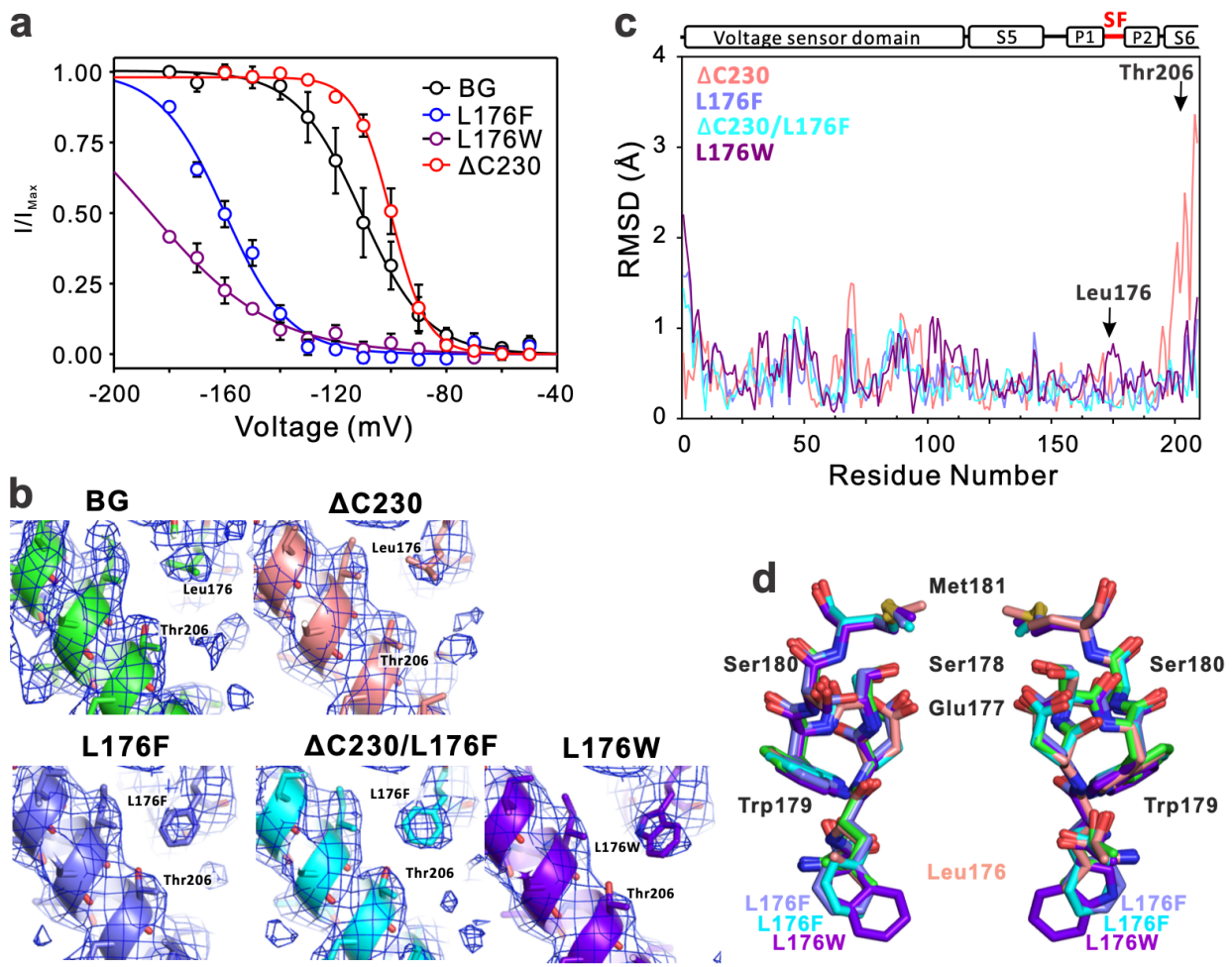


**Figure 2. Mutations at the selectivity filter or C-terminus change the inactivation of the NavAb channel**

**a**. Steady-state inactivation of NavAb BG, L176F, L176W, and ΔC230 mutants. **b**. The electron density map of BG, L176F, ΔC230 and ΔC230/L176F mutants around L176 in the selectivity filter and T206 in the S6 helix. The $2F_O - F_C$ electron density map contoured at 1σ (blue mesh) shows the proximity between the S6 helix and the selectivity filter. **c**. Root Mean Square Deviation (RMSD) of pore domain residues of mutant channels against NavAb BG mutant carrying only the N49K background mutation. **d**. Superimposition of the selectivity filter of crystal structures of the BG, L176F, L176W, ΔC230 and ΔC230/L176F mutants.

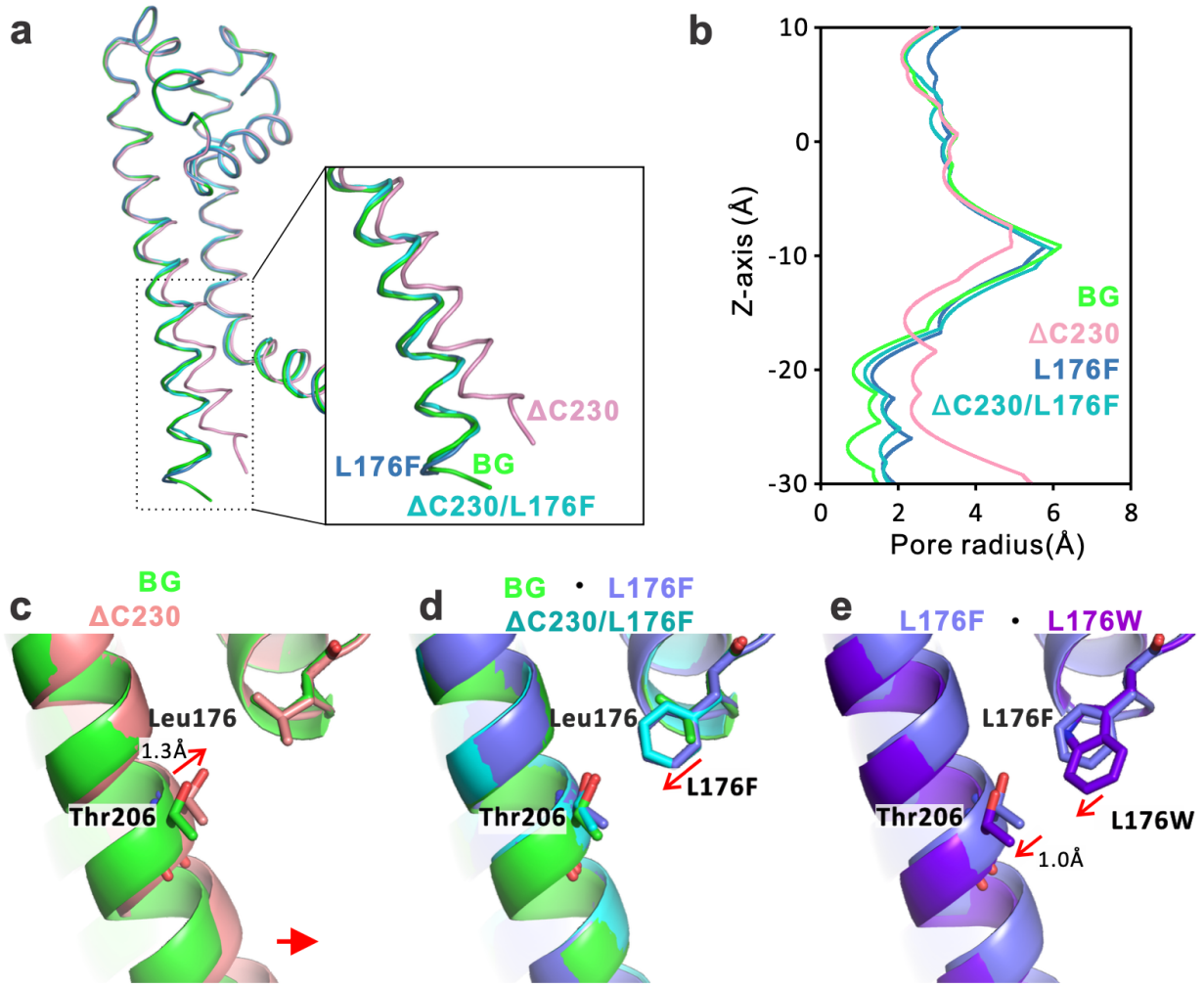


**Figure 3. The selectivity filter structure and communication between the S6 helix and the selectivity filter**

**a**. Superimposition of the pore domains of NavAb BG, L176F, ΔC230 and ΔC230/L176F mutants. **b**. Pore diameter profiles of NavAb BG, L176F, ΔC230 and ΔC230/L176F mutants. **c**. Superimposition of the selectivity filter and the S6 helix of BG and ΔC230 mutants. **d**. Superimposition of the selectivity filter and the S6 helix of BG, L176F and ΔC230/L176F mutants. **e**. Superimposition of the selectivity filter and the S6 helix of L176F and L176W mutants.

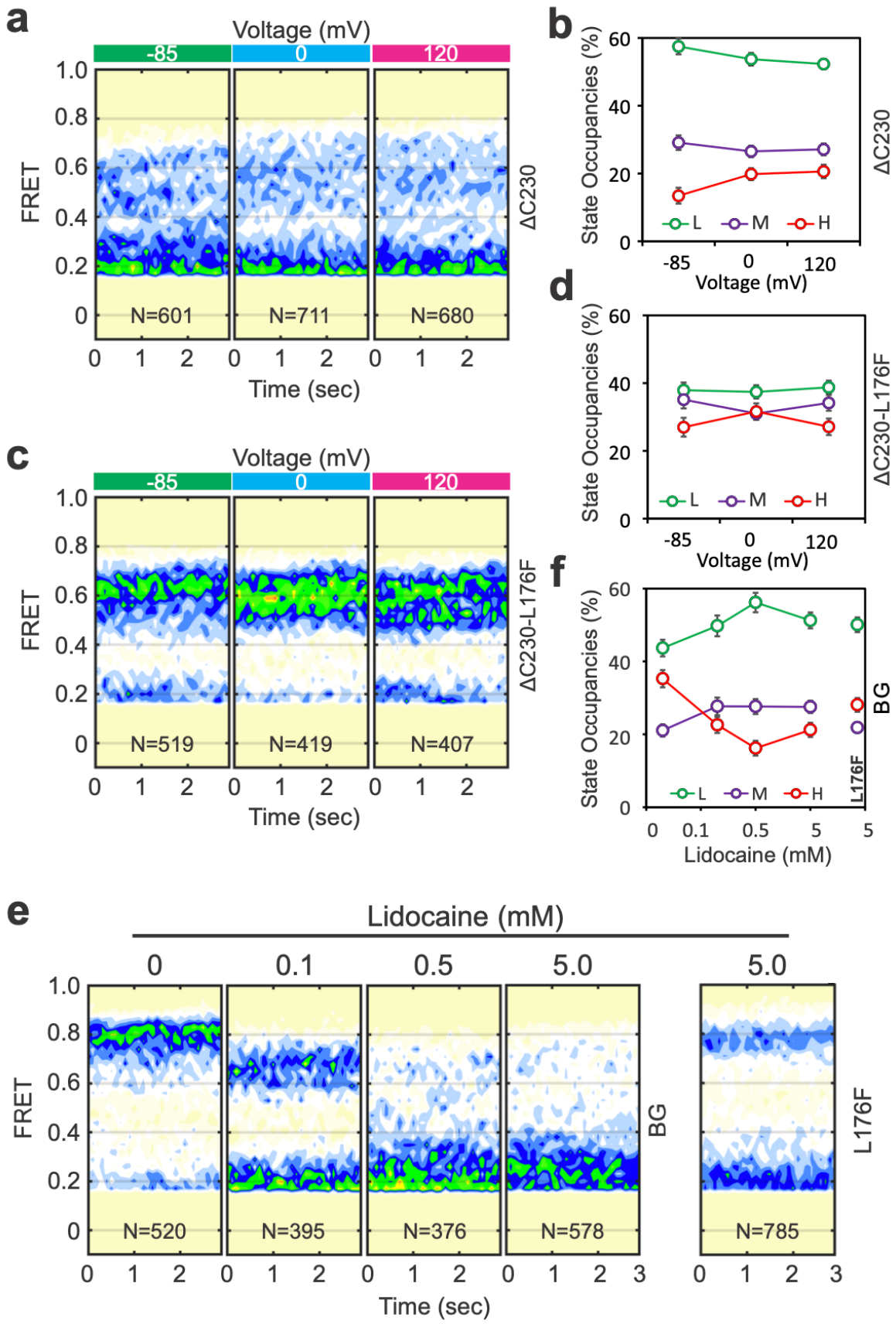
a
Voltage (mV)
-85
0
120
FRET
N=601
N=711
N=680
Time (sec)
ΔC230
b
State Occupancies (%)
L
M
H
Voltage (mV)
ΔC230
c
Voltage (mV)
-85
0
120
FRET
N=519
N=419
N=407
Time (sec)
ΔC230-L176F
d
State Occupancies (%)
L
M
H
Voltage (mV)
ΔC230-L176F
f
State Occupancies (%)
L
M
H
L176F
BG
Lidocaine (mM)
e
Lidocaine (mM)
0
0.1
0.5
5.0
5.0
FRET
N=520
N=395
N=376
N=578
N=785
Time (sec)
BG
L176F

1

**Figure 4. Crosstalk between the C-terminal primary gate and the selectivity filter**

**a**-**d**. Contour maps (**a**, **c**) and FRET state occupancies (**b**, **d**) of smFRET data collected from V190C labeling sites carrying the ΔC230 C-terminal deletion, without (**a**, **b**) or with (**c**, **d**) the L176F mutation, under -85, 0, and 120 mV. Contour maps of smFRET data collected from V190C labeling sites carrying the ΔC230 C-terminal deletion and L176F mutation. **e-f**. Contour maps (**e**) and FRET state occupancies (**f**) of the smFRET data collected from the V190C labeling sites without (BG) or with the L176F mutation in the presence of different concentrations of lidocaine under 0 mV. Lidocaine was shown to deplete the high FRET population in a dose-dependent manner, while the L176F mutation, which enhances slow inactivation, restored the high FRET conformation of the selectivity filter.

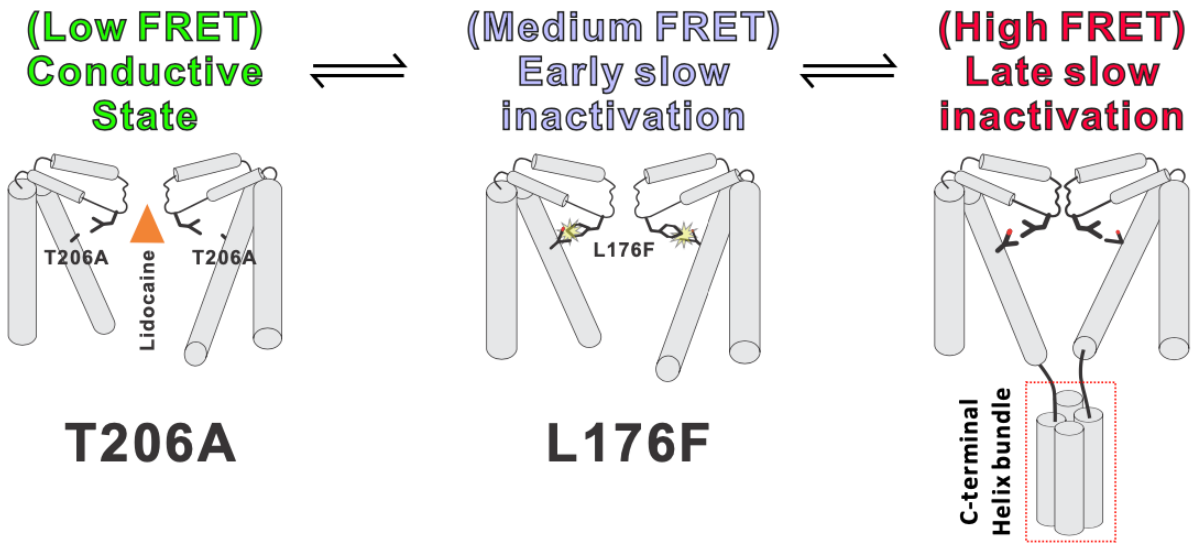


**Figure 5. Conformational transitions in the NavAb selectivity filter from conductive state to early and late inactivated states revealed by smFRET measurements**

The low, medium, and high FRET populations correspond to the dilated/conductive, intermediate/early and constricted/late slow inactivation states, respectively. T206A, lidocaine, and C-terminal deletion enriched conductive state conformations, while L176F, C-terminal helix bundle and activating voltages promoted early and late slow inactivated state conformations. Only the pore domains of two subunits were shown, with the front and rear subunits removed for clarity.

1 **Extended Table 1. Data collection and refinement statistics.**

| | BG(N49K) | L176F | L176W | ΔC230 | ΔC230/ L176F |
|---|---|---|---|---|---|
| **PDB code** | 9VDQ | 9VDR | 9VDS | 9VDT | 9VDU |
| **Wavelength** | | | | | |
| **Resolution range** | 41 - 3.1 (3.2-3.1) | 30 - 3.7 (3.8-3.7) | 30 - 3.7 (3.8-3.7) | 29.7- 3.5 (3.6-3.5) | 29.3 - 3.4 (3.5 - 3.4) |
| **Space group** | I 4 2 2 | I 4 2 2 | I 4 2 2 | I 4 2 2 | I 4 2 2 |
| **Unit cell** | 127.2<br>127.2<br>201.4<br>90<br>90<br>90 | 125.3<br>125.3<br>202.4<br>90<br>90<br>90 | 126.9<br>126.9<br>204.9<br>90<br>90<br>90 | 129.8<br>129.8<br>200.3<br>90<br>90<br>90 | 128.5<br>128.5<br>200.8<br>90<br>90<br>90 |
| **Total reflections** | 224672 (22772) | 694500 (66886) | 503654 (49820) | 290487 (29476) | 1247544 (119374) |
| **Unique reflections** | 15361 (1079) | 8934 (828) | 9266 (869) | 11127 (980) | 11918 (1085) |
| **Multiplicity** | 14.6 (15.0) | 77.7 (76.6) | 54.4 (55.4) | 26.1 (27.2) | 104.7 (103.9) |
| **Completeness (%)** | 96.15 (71.03) | 99.03 (94.85) | 99.30 (96.66) | 98.75 (90.49) | 99.15 (94.43) |
| **Mean I/sigma(I)** | 21.38 (1.95) | 31.17 (5.09) | 26.57 (4.83) | 27.92 (3.01) | 24.75 (3.44) |
| **Wilson B-factor** | 65.66 | 108.33 | 152.50 | 97.64 | 88.46 |
| **R-merge** | 0.129 (1.63) | 0.09663 (1.506) | 0.1034 (3.198) | 0.08158 (1.253) | 0.3232 (3.816) |
| **R-meas** | 0.1336 (1.682) | 0.0975 (1.516) | 0.1052 (3.228) | 0.08338 (1.277) | 0.3249 (3.834) |
| **R-pim** | 0.03479 (0.4332) | 0.01217 (0.1726) | 0.01715 (0.4321) | 0.01678 (0.2434) | 0.03249 (0.3729) |

| | | | | | |
|---|---|---|---|---|---|
| **CC1/2** | 0.999 (0.886) | 1 (0.994) | 1 (0.986) | 0.999 (0.979) | 0.985 (0.932) |
| **CC*** | 1 (0.969) | 1 (0.999) | 1 (0.996) | 1 (0.995) | 0.996 (0.982) |
| **Reflections used in refinement** | 14806 (1079) | 8880 (828) | 9236 (869) | 11025 (980) | 11854 (1085) |
| **Reflections used for R-free** | 1479 (107) | 420 (33) | 434 (38) | 539 (50) | 574 (45) |
| **R-work** | 0.2412 (0.2937) | 0.2976 (0.2938) | 0.3129 (0.3451) | 0.3084 (0.2724) | 0.2538 (0.2460) |
| **R-free** | 0.2893 (0.3574) | 0.3273 (0.4450) | 0.3389 (0.4130) | 0.3444 (0.3100) | 0.3039 (0.2700) |
| **CC(work)** | 0.826 (0.606) | 0.955 (0.564) | 0.971 (0.450) | 0.897 (0.721) | 0.917 (0.698) |
| **CC(free)** | 0.795 (0.543) | 0.784 (0.206) | 0.886 (0.286) | 0.592 (0.430) | 0.838 (0.614) |
| **Number of non-hydrogen atoms** | 2281 | 2044 | 1866 | 2225 | 2155 |
| **macromolecules** | 1870 | 1832 | 1798 | 1784 | 1795 |
| **ligands** | 401 | 207 | 68 | 436 | 355 |
| **solvent** | 10 | 5 | | 5 | 5 |
| **Protein residues** | 229 | 223 | 218 | 217 | 218 |
| **RMS(bonds)** | 0.012 | 0.004 | 0.003 | 0.003 | 0.010 |
| **RMS(angles)** | 1.32 | 0.71 | 0.48 | 0.76 | 1.27 |
| **Ramachandran favored** | 99.12 | 99.09 | 98.13 | 100.00 | 99.53 |

| | | | | | |
|---|---|---|---|---|---|
| **(%)** | | | | | |
| **Ramachandran allowed (%)** | 0.88 | 0.91 | 1.87 | 0.00 | 0.47 |
| **Ramachandran outliers (%)** | 0.00 | 0.00 | 0.00 | 0.00 | 0.00 |
| **Rotamer outliers (%)** | 0.96 | 0.00 | 0.00 | 0.00 | 0.00 |
| **Clashscore** | 15.07 | 9.39 | 6.25 | 9.88 | 13.98 |
| **Average B-factor** | 68.96 | 124.66 | 163.57 | 126.84 | 89.12 |
| **macromolecules** | 66.25 | 124.28 | 163.14 | 122.92 | 84.98 |
| **ligands** | 82.04 | 129.62 | 174.95 | 143.39 | 110.53 |
| **solvent** | 51.69 | 58.92 | | 79.99 | 55.06 |
| **Number of TLS groups** | 1 | 1 | 1 | 1 | 1 |

Statistics for the highest-resolution shell are shown in parentheses.

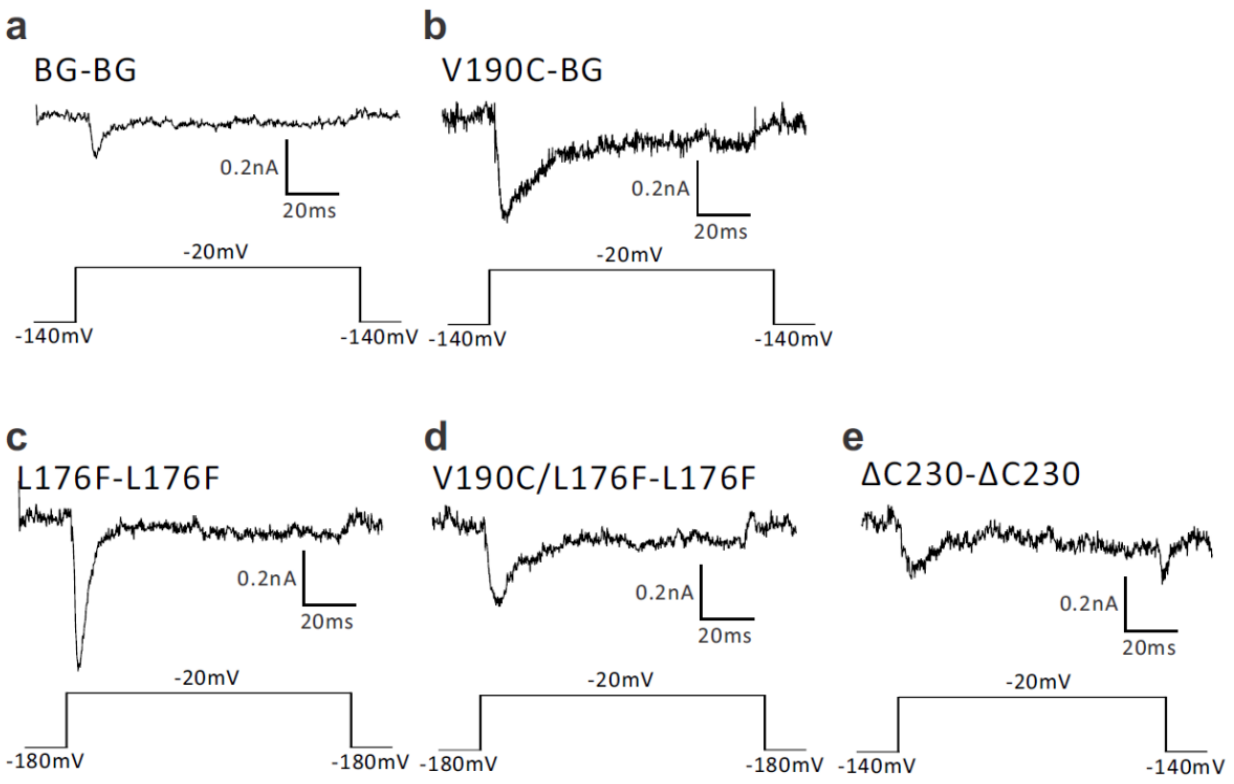


**Extended Figure 1. The channel activity of NavAb tandem dimers**

Representative trace of NavAb (**a**) BG dimer carrying only the N49K background mutation, (**b**) BG dimer with additional V190C in first subunit, (**c**) BG dimer with additional L176F mutation in both subunits, (**d**) BG dimer with additional L176F mutation in both subunits and V190C in first subunit, and (**e**) BG dimer with C-terminal deletion ΔC230 in both subunits. All currents were generated by stimulation pulses of -20 mV.

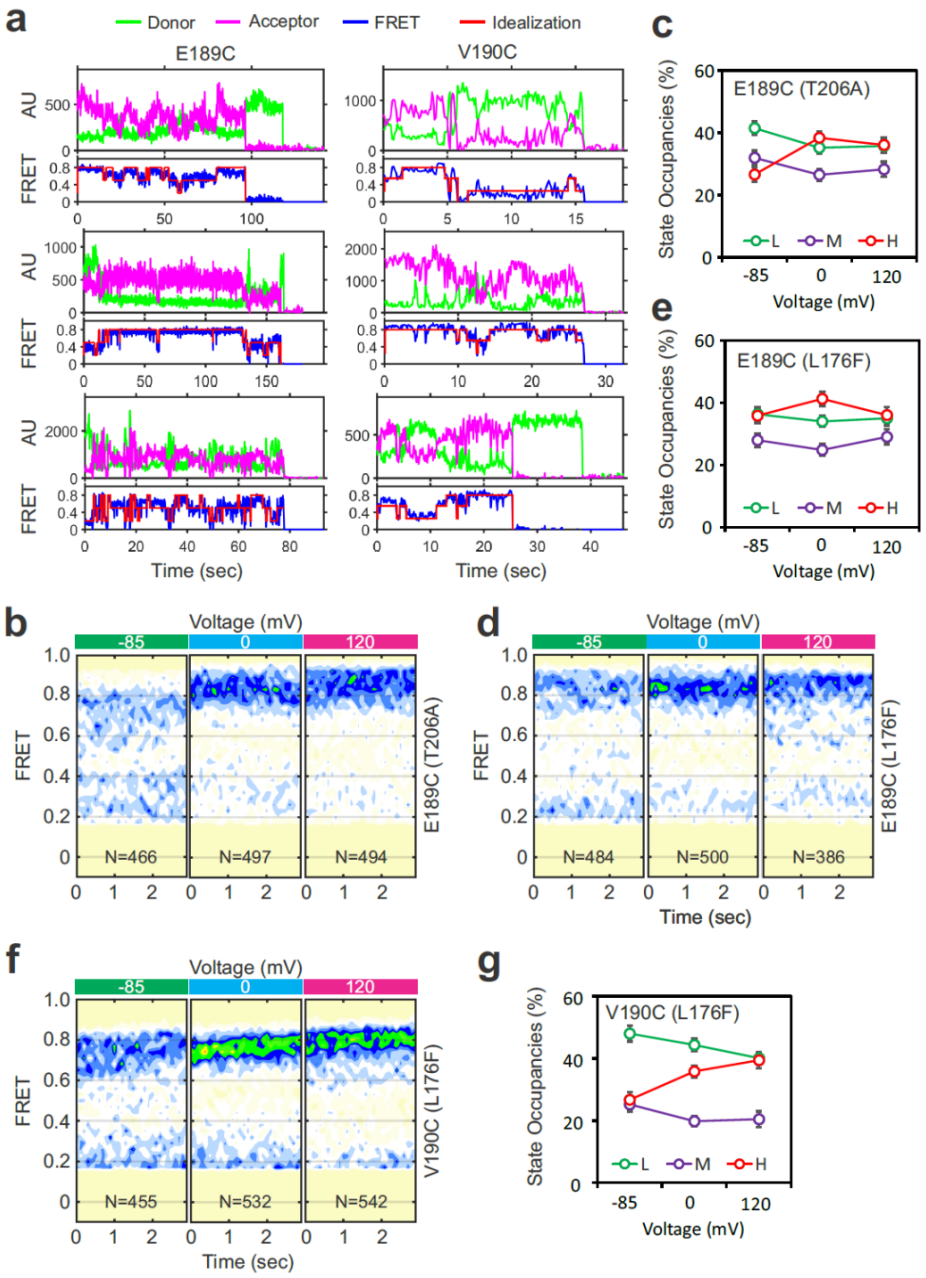


**Extended Figure 2. Activating voltage induces the constricted conformation at the NavAb selectivity filter at the potential inactivation state**

**a**. Representative smFRET traces exhibiting conformational transitions among 3 different states; **b-g**. Contour maps (**b**, **d** and **f**) and FRET state occupancies (**c**, **e** and **g**) of smFRET data collected from either E189C (**b**, **c**, **d** and **e**) or V190C (**f** and **g**) labeling

sites carrying either L176F (**d**, **e**, **f** and **g**) or T206A (**b** and **c**) background mutations, under -85, 0 and 120 mV.

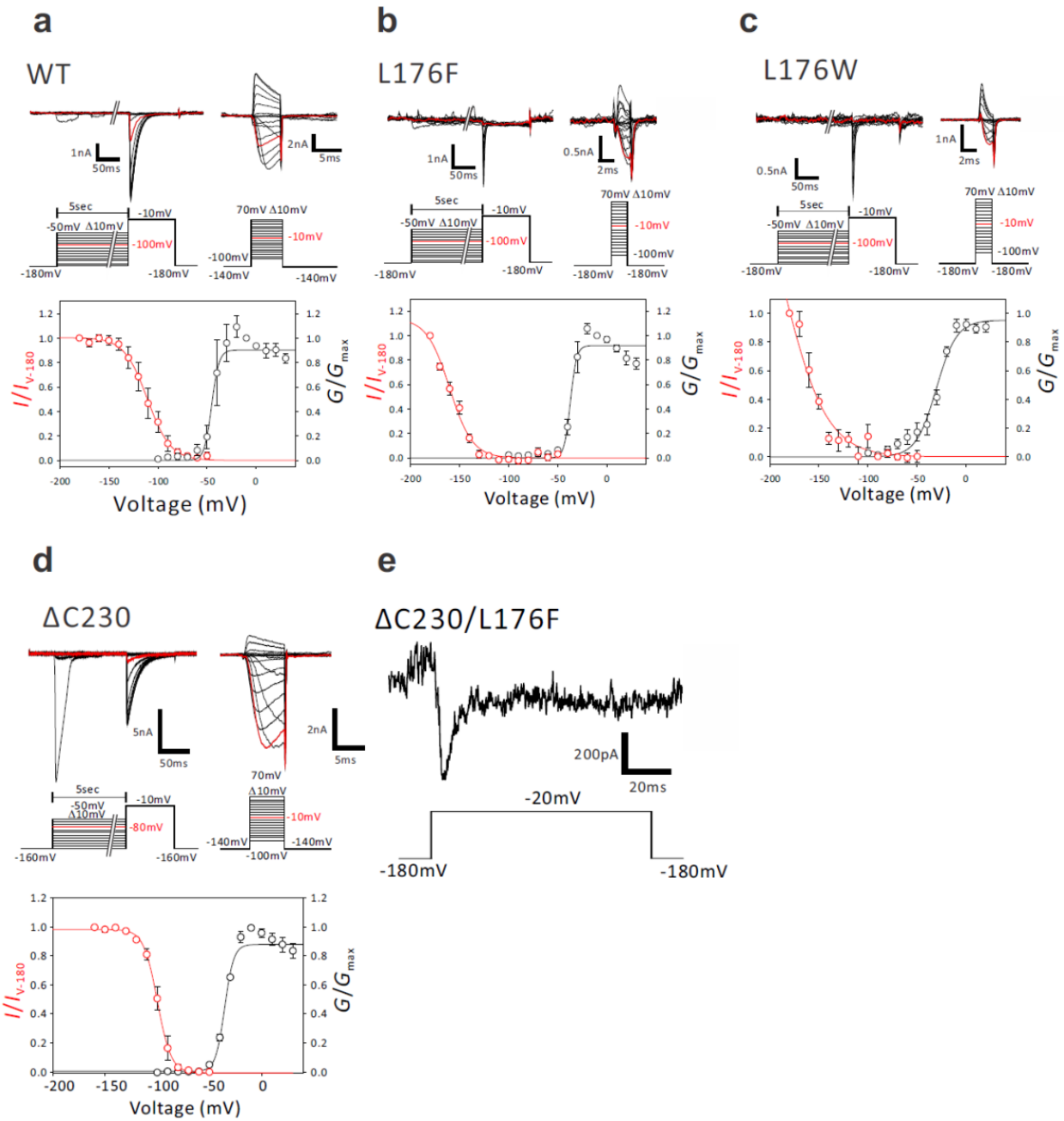


**Extended Figure 3. Voltage-dependent activation and inactivation of BG, L176F, L176W, ΔC230 and ΔC230/L176F mutants.**

**a-d**. Representative traces of deactivation tail currents and steady-state inactivation, and voltage-dependency of activation and inactivation of BG, L176F, L176W and ΔC230 mutants. **e**. Representative trace of the ΔC230/L176F current generated by stimulation pulses of -20 mV.

## References


1. Hille, B. *Ion channels of excitable membranes*, xviii, 814 p. (Sinauer Associates Inc., Sunderland, MA USA, 2001).
2. de Lera Ruiz, M. & Kraus, R.L. Voltage-Gated Sodium Channels: Structure, Function, Pharmacology, and Clinical Indications. *J Med Chem* **58**, 7093-118 (2015).
3. Huang, J., Pan, X. & Yan, N. Structural biology and molecular pharmacology of voltage-gated ion channels. *Nat Rev Mol Cell Biol* **25**, 904-925 (2024).
4. Catterall, W.A., Lenaeus, M.J. & Gamal El-Din, T.M. Structure and Pharmacology of Voltage-Gated Sodium and Calcium Channels. *Annu Rev Pharmacol Toxicol* **60**, 133-154 (2020).
5. Ulbricht, W. Sodium channel inactivation: molecular determinants and modulation. *Physiol Rev* **85**, 1271-301 (2005).
6. Jiang, D. et al. Open-state structure and pore gating mechanism of the cardiac sodium channel. *Cell* **184**, 5151-5162 e11 (2021).
7. Silva, J. Slow inactivation of Na(+) channels. *Handb Exp Pharmacol* **221**, 33-49 (2014).
8. Payandeh, J. & Minor, D.L., Jr. Bacterial voltage-gated sodium channels (BacNa(V)s) from the soil, sea, and salt lakes enlighten molecular mechanisms of electrical signaling and pharmacology in the brain and heart. *J Mol Biol* **427**, 3-30 (2015).
9. Ren, D. et al. A prokaryotic voltage-gated sodium channel. *Science* **294**, 2372-5 (2001).
10. Payandeh, J., Scheuer, T., Zheng, N. & Catterall, W.A. The crystal structure of a voltage-gated sodium channel. *Nature* **475**, 353-8 (2011).
11. Wisedchaisri, G. et al. Resting-State Structure and Gating Mechanism of a Voltage-Gated Sodium Channel. *Cell* **178**, 993-1003 e12 (2019).
12. Chen, H. et al. Structural mechanism of voltage-gated sodium channel slow inactivation. *Nat Commun* **15**, 3691 (2024).
13. Payandeh, J., Gamal El-Din, T.M., Scheuer, T., Zheng, N. & Catterall, W.A. Crystal structure of a voltage-gated sodium channel in two potentially inactivated states. *Nature* **486**, 135-9 (2012).
14. Gamal El-Din, T.M., Martinez, G.Q., Payandeh, J., Scheuer, T. & Catterall, W.A. A gating charge interaction required for late slow inactivation of the bacterial sodium channel NavAb. *J Gen Physiol* **142**, 181-90 (2013).
15. Pavlov, E. et al. The pore, not cytoplasmic domains, underlies inactivation in a prokaryotic sodium channel. *Biophys J* **89**, 232-42 (2005).
16. Gamal El-Din, T.M., Lenaeus, M.J., Ramanadane, K., Zheng, N. & Catterall, W.A. Molecular dissection of multiphase inactivation of the bacterial sodium channel Na(V)Ab. *J Gen Physiol* **151**, 174-185 (2019).
17. Payandeh, J. Progress in understanding slow inactivation speeds up. *J Gen Physiol* **150**, 1235-1238 (2018).
18. Han, S. et al. Voltage sensor dynamics of a bacterial voltage-gated sodium channel NavAb reveal three conformational states. *J Biol Chem* **299**, 102967 (2023).

19. Han, S. et al. Cholesterol inhibits human voltage-gated proton channel hHv1. *Proc Natl Acad Sci U S A* **119**, e2205420119 (2022).
20. Han, S. et al. Structural dynamics determine voltage and pH gating in human voltage-gated proton channel. *Elife* **11**(2022).
21. Lenaeus, M.J. et al. Structures of closed and open states of a voltage-gated sodium channel. *Proc Natl Acad Sci U S A* **114**, E3051-E3060 (2017).
22. Irie, K., Shimomura, T. & Fujiyoshi, Y. The C-terminal helical bundle of the tetrameric prokaryotic sodium channel accelerates the inactivation rate. *Nat Commun* **3**, 793 (2012).
23. Sheets, P.L., Jarecki, B.W. & Cummins, T.R. Lidocaine reduces the transition to slow inactivation in Na(v)1.7 voltage-gated sodium channels. *Br J Pharmacol* **164**, 719-30 (2011).
24. Sandtner, W. et al. Lidocaine: a foot in the door of the inner vestibule prevents ultra-slow inactivation of a voltage-gated sodium channel. *Mol Pharmacol* **66**, 648-57 (2004).
25. Gamal El-Din, T.M., Lenaeus, M.J., Zheng, N. & Catterall, W.A. Fenestrations control resting-state block of a voltage-gated sodium channel. *Proc Natl Acad Sci U S A* **115**, 13111-13116 (2018).
26. Cuello, L.G., Jogini, V., Cortes, D.M. & Perozo, E. Structural mechanism of C-type inactivation in K(+) channels. *Nature* **466**, 203-8 (2010).
27. Cuello, L.G. et al. Structural basis for the coupling between activation and inactivation gates in K(+) channels. *Nature* **466**, 272-5 (2010).
28. Wang, S. et al. Potassium channel selectivity filter dynamics revealed by single-molecule FRET. *Nat Chem Biol* **15**, 377-383 (2019).
29. Catterall, W.A. Voltage-gated sodium channels at 60: structure, function and pathophysiology. *J Physiol* **590**, 2577-89 (2012).
30. Irie, K., Haga, Y., Shimomura, T. & Fujiyoshi, Y. Optimized expression and purification of NavAb provide the structural insight into the voltage dependence. *FEBS Lett* **592**, 274-283 (2018).
31. Irie, K., Oda, Y., Sumikama, T., Oshima, A. & Fujiyoshi, Y. The structural basis of divalent cation block in a tetrameric prokaryotic sodium channel. *Nat Commun* **14**, 4236 (2023).
32. Hirata, K. et al. ZOO: an automatic data-collection system for high-throughput structure analysis in protein microcrystallography. *Acta Crystallogr D Struct Biol* **75**, 138-150 (2019).
33. Yamashita, K., Hirata, K. & Yamamoto, M. KAMO: towards automated data processing for microcrystals. *Acta Crystallogr D Struct Biol* **74**, 441-449 (2018).
34. Kabsch, W. Xds. *Acta Crystallogr D Biol Crystallogr* **66**, 125-32 (2010).
35. Tickle, I.J., Flensburg, C., Keller, P., Paciorek, W., Sharff, A., Vonrhein, C., Bricogne, G. . STARANISO. *(http://staraniso.globalphasing.org/cgi-bin/staraniso.cgi)* **Cambridge, United Kingdom: Global Phasing Ltd.**(2016).
36. McCoy, A.J. et al. Phaser crystallographic software. *J Appl Crystallogr* **40**, 658-674 (2007).
37. Emsley, P., Lohkamp, B., Scott, W.G. & Cowtan, K. Features and development of Coot. *Acta Crystallogr D Biol Crystallogr* **66**, 486-501 (2010).

38. Adams, P.D. et al. PHENIX: a comprehensive Python-based system for macromolecular structure solution. *Acta Crystallogr D Biol Crystallogr* **66**, 213-21 (2010).
39. Winn, M.D. et al. Overview of the CCP4 suite and current developments. *Acta Crystallogr D Biol Crystallogr* **67**, 235-42 (2011).
40. Smart, O.S., Neduvelil, J.G., Wang, X., Wallace, B.A. & Sansom, M.S. HOLE: a program for the analysis of the pore dimensions of ion channel structural models. *J Mol Graph* **14**, 354-60, 376 (1996).
41. Altman, R.B. et al. Cyanine fluorophore derivatives with enhanced photostability. *Nat Methods* **9**, 68-71 (2011).
42. Joo, C. & Ha, T. Preparing sample chambers for single-molecule FRET. *Cold Spring Harb Protoc* **2012**, 1104-8 (2012).
43. Aitken, C.E., Marshall, R.A. & Puglisi, J.D. An oxygen scavenging system for improvement of dye stability in single-molecule fluorescence experiments. *Biophys J* **94**, 1826-35 (2008).
44. Juette, M.F. et al. Single-molecule imaging of non-equilibrium molecular ensembles on the millisecond timescale. *Nat Methods* **13**, 341-4 (2016).
45. Qin, F., Auerbach, A. & Sachs, F. Hidden Markov modeling for single channel kinetics with filtering and correlated noise. *Biophys J* **79**, 1928-44 (2000).